JGR Space Physics

RESEARCH ARTICLE
10.1029/2022JA030489

Determining Latitudinal Extent of Energetic Electron Precipitation Using MEPED On-Board NOAA/POES

E. M. Babu[1], H. Nesse Tyssøy[1], C. Smith-Johnsen[1], V. Maliniemi[1], J. A. Salice[1], R. M. Millan[2], and I. G. Richardson[3,4]

[1]Department of Physics and Technology, Birkeland Centre for Space Science, University of Bergen, Bergen, Norway, [2]Department of Physics and Astronomy, Dartmouth College, Hanover, NH, USA, [3]Heliophysics Science Division, NASA Goddard Space Flight Center, Greenbelt, MD, USA, [4]Department of Astronomy, University of Maryland, College Park, MD, USA

Key Points:

- A model predicting equatorward extent of >43 keV electron precipitation is developed based on pressure-corrected Dst
- The model has an error estimate of ±2.2° cgmlat over a full solar cycle (2004–2014)
- The model has the highest accuracy during periods dominated by high-speed solar wind streams

Correspondence to:
E. M. Babu,
Eldho.Babu@uib.no

Citation:
Babu, E. M., Tyssøy, H. N., Smith-Johnsen, C., Maliniemi, V., Salice, J. A., Millan, R. M., & Richardson, I. G. (2022). Determining latitudinal extent of energetic electron precipitation using MEPED on-board NOAA/POES. *Journal of Geophysical Research: Space Physics*, *127*, e2022JA030489. https://doi.org/10.1029/2022JA030489

Received 24 MAR 2022
Accepted 14 SEP 2022

Abstract Energetic Electron Precipitation (EEP) from the plasma sheet and the radiation belts ionizes the polar lower thermosphere and mesosphere. EEP increases the production of NO_x and HO_x, which will catalytically destroy ozone, an important element of atmospheric dynamics. Therefore, measurement of the latitudinal extent of the precipitation boundaries is important in quantifying the atmospheric effects of the Sun-Earth interaction. This study uses measurements by the Medium Energy Proton Electron Detector (MEPED) of six NOAA/POES and EUMETSAT/METOP satellites from 2004 to 2014 to determine the latitudinal boundaries of EEP and their variability with geomagnetic activity and solar wind drivers. Variation of the boundaries for different electron energies and Magnetic Local Time (MLT) is studied. Regression analyses are applied to determine the best predictor variable based on solar wind parameters and geomagnetic indices. The highest correlation was found for the pressure-corrected Dst index when applying a linear regression model. A model of the equatorward EEP boundary is developed separately for three different energy channels, >43, >114, and >292 keV, and for 3 hour MLT sectors. For >43 keV EEP, 80% of the equatorward boundaries predicted by the model are within ±2.2° cgmlat. The model exhibits a solar cycle bias where it systematically exaggerates the equatorward movement of the EEP region during solar minimum. The highest accuracy of the model is found in periods dominated by corotating interaction regions/high speed solar wind streams. The result will be a key element for constructing a model of EEP variability to be applied in atmosphere climate models.

Plain Language Summary Charged particles trapped in the Earth's magnetic field get accelerated to high energies through various magnetospheric processes. They can eventually precipitate into the Earth's atmosphere in a process known as Energetic Electron Precipitation or EEP. EEP deposits energy in the mesosphere and lower thermosphere which increase the production of ozone-depleting substances. Vertical transport of these, in particular during winter, can lead to indirect destruction of stratospheric ozone, a crucial element of atmospheric dynamics. Therefore, measurement of the latitudinal extent of EEP is important in quantifying the atmospheric effects of the Sun-Earth interaction. We use measurements from six NOAA/POES and EUMETSAT/METOP satellites from 2004 to 2014 to determine the equatorward latitudinal boundaries of EEP. We investigate how they correlate with solar wind parameters and geomagnetic indices to identify the best predictor for EEP boundaries. The result will be a key element for constructing a model of EEP variability to be applied in atmosphere climate models.

1. Introduction

Near-Earth space is permeated by solar plasma, driven by the slow solar winds, Coronal Mass Ejections (CMEs) or High-speed Solar wind Streams (HSSs) (Borovsky & Denton, 2006). CMEs are enormous plasma eruptions commonly caused by stressed magnetic fields around sunspots resulting in the most powerful geomagnetic storms. HSSs originate from coronal holes on the Sun. As the HSSs catch up with the slow solar wind, compression regions form, known as Co-rotating Interaction Regions (CIRs) (Richardson, 2018). Although the HSS/CIR geomagnetic disturbances typically are not as strong as CMEs, they often produce longer disturbed conditions in the near-Earth space (Zhang et al., 2007). The energetic electrons and ions from the solar wind and from the Earth's ionosphere gets trapped in the Earth's magnetosphere and forms torus-shaped regions (Shelley et al., 1972; Van Allen, 1959) constituting the radiation belts or the Van Allen belts. Investigating these trapped

particles have been a matter of interest since its discovery in 1958. Charged particles will be accelerated in the inner magnetosphere to significantly higher energy levels than in the solar wind by wave-particle accelerations and inward radial diffusion (Friedel et al., 2002).

There are two sinks that prompt loss of plasma from the radiation belts. The first is loss through the magnetopause back into the solar wind. The second sink is the atmosphere. Magnetospheric perturbations from plasma instabilities, pitch-angle anisotropy, and gradients in temperature and density generate plasma waves causing pitch-angle scattering of trapped particles into the atmospheric loss cone (Millan & Thorne, 2007), where they collide with atmospheric gases and deposit their energy.

Precipitating medium-energy electrons (MEE) (≥30 keV) amplify the local production of odd nitrogen (NO_x: N, NO, NO_2) and odd hydrogen (HO_x: H, OH, HO_2). NO_x can live sufficiently long in polar winter to be transported down to stratospheric altitudes affecting stratospheric ozone (Damiani et al., 2016; Maliniemi et al., 2021; Solomon et al., 1982), while HO_x have the capability of disrupting the mesospheric ozone balance (Andersson et al., 2012; Verronen et al., 2011; Zawedde et al., 2019). These chemical processes can impact the atmospheric temperature and dynamics, the consequences of which, might map down to the troposphere and surface (Baumgaertner et al., 2011; Maliniemi et al., 2019; Seppälä et al., 2009). Therefore, quantification of energetic electron precipitation (EEP), particularly its MEE aspect, is important in terms of understanding the impact of the Sun on the Earth's climate.

An accurate quantification of the MEE precipitation will require a solid description of both the overall MEE intensity, as well as its latitudinal extent. The plasmapause location is considered to play a critical role in determining the equatorward boundary of the MEE precipitation region (Moldwin et al., 2002; Pierrard et al., 2021, and references therein). It marks the outer boundary of the dense cold plasma in the plasmasphere. As the properties of electromagnetic waves strongly depend on the medium they propagate in, the plasmapause marks an abrupt change in the characteristics of the wave-particle interaction, and hence the radiation belt MEE diffusion rate into the atmospheric loss cone (Moldwin et al., 2002; Pierrard et al., 2021; Whittaker et al., 2014, and references therein). Chorus waves are dominating the EEP processes outside of the plasmasphere (Whittaker et al., 2014). Electromagnetic Ion Cyclotron (EMIC) wave-driven precipitation processes are favorable close to the outer edge of the plasmasphere (Carson et al., 2013), while plasmaspheric hiss are expected to be responsible for weak MEE precipitating fluxes within the plasmasphere (Hardman et al., 2015), as are lightning-generated whistlers (Rodger et al., 2007; Voss et al., 1998). The plasmapause location can vary strongly with geomagnetic activity, which implies a corresponding change in the equatorward boundary of the MEE precipitation.

Recently, van de Kamp et al. (2016) and van de Kamp et al. (2018) developed a MEE atmospheric ionization-rate model (>30 keV) based on an empirically derived plasmapause location, geomagnetic activity, and observations based on the Medium Energy Proton Electron Detector (MEPED) 0° telescopes on-board the National Oceanic and Atmospheric Administration (NOAA), Polar Orbiting Environmental Satellites (POES), and ESA's Meteorological Operational (MetOp) Satellites. The same observations have been used by Shekhar et al. (2017) and Gasque et al. (2021) to statistically determine the spatial extent of precipitating relativistic electrons (>800 keV). At high to mid-latitudes the MEPED 0° telescopes detect precipitating particle fluxes, whereas the 90° telescopes detect precipitating particle fluxes and/or trapped particles in the radiation belts (Nesse Tyssøy et al., 2016; Rodger et al., 2010). In the common case of pitch angle anisotropy, the 0° telescopes will underestimate, while the 90° telescopes will overestimate the flux of precipitating electrons (Nesse Tyssøy et al., 2016; Tyssøy et al., 2019). Hence, an accurate determination of the precipitation region will require the ability to estimate the MEE precipitating fluxes also during weak pitch angle diffusion. In this study, we combine observations from both the MEPED 0° and 90° detectors together with the theory of pitch angle diffusion by wave-particle interaction to quantify the MEE flux in the Bounce Loss Cone (BLC). At a specific latitude the size of the BLC changes with longitude due to the variation in the magnetic field strength. Over one drift period, the largest BLC will correspond to the drift loss cone. Applying the BLC compared to drift loss cone enables assessment of longitudinal differences and prevents overestimation of the precipitation at regions where the BLC is small. Also, as the level of anisotropy will vary with energy, we treat the MEPED energy channels, >43, >114, and >292 keV independently. We determine the equatorward boundary of the MEE precipitation region on a daily scale over a full solar cycle from 2004 to 2014 for different MLTs. We explore its dependency on solar wind components and geomagnetic activity. The parameter giving the highest predictability is used to develop a model which will be a key element for constructing a model of MEE variability to be applied in chemistry-climate models. The paper

is organized as follows: Section 2 describes the electron count measurements and the method to estimate the precipitating fluxes. Section 3 outlines the process of identifying the equatorward boundaries, whereas Section 4 examines its correlation with solar wind parameters and geomagnetic indices. The subsequent model and its accuracy is presented in Section 5.

2. Data

The Space Environment Monitor (SEM) on-board the NOAA/POES and EUMETSAT/MetOp series have been measuring precipitating and trapped electron and proton fluxes since 1978, covering roughly four solar cycles. These satellites have a circular sun-synchronous polar orbit with an orbital period of approximately 102 min (Evans & Greer, 2000). Each satellite covers similar MLT regions in every pass while moving through the L-shells. Their orbital altitude of 800–850 km from the surface of the Earth with a stabilized spatial orientation (Evans & Greer, 2000), allows them to monitor both trapped and precipitating particles near the foot of the field lines (Rodger et al., 2010; Nesse Tyssøy et al., 2016).

For this study, we use the MEPED on-board the second-generation SEM-2 instrument package which commenced its operation in 1998. The MEPED instrument has two solid-state detectors (0° and 90°) to measure a wide energy range of protons and electrons (Evans & Greer, 2000). This study concerns energetic electrons and therefore, uses readings from the electron telescopes. The MEPED electron telescopes have three energy channels E1, E2, and E3 measuring integral electron fluxes with nominal energy values of >30, >100, and >300 keV, respectively. Yando et al. (2011), however, demonstrated that the real detector efficiency will strongly depend on the incoming energy spectrum. Ødegaard et al. (2017) utilized the geometric factors given in Yando et al. (2011) to determine new optimized effective integral energy limits >43, >114, and >292 keV and associated geometric factors based on a series of realistic power law and exponential spectra. Furthermore, the electron energy channels suffer from >210 keV proton contamination (Evans & Greer, 2000; Yando et al., 2011) which results in false counts if used without rectification. We first apply the proton correction factors obtained by Sandanger et al. (2015) and Ødegaard et al. (2016) before fitting a monotonic piecewise cubic Hermite interpolating polynomial to the observed proton fluxes. The proton flux in the energy ranges known to impact the respective electron channels (Evans & Greer, 2000) is then retrieved and subtracted from the originally measured electron fluxes.

The 0° detector points toward the local zenith and measures particles near the center of the atmospheric BLC at high latitudes while the 90° detector, mounted orthogonally to the 0° detector and antiparallel to the spacecraft velocity vector, quantifies a combination of particles inside and outside the atmospheric BLC (Evans & Greer, 2000; Meredith et al., 2011; Nesse Tyssøy et al., 2016; Rodger et al., 2010). Consequently, using either the 0° or the 90° detector alone for this study will be an under-estimate or an over-estimate, respectively. We account for this by combining fluxes from both the 0° and 90° telescopes together with electron pitch angle distributions from the theory of wave-particle interactions in the magnetosphere. We solve the Fokker-Planck equation for particle diffusion (Kennel & Petschek, 1966; Theodoridis & Paolini, 1967) for a wide range of diffusion coefficients (the specific equations are also given in Nesse Tyssøy et al., 2016). The solutions are then transformed to the satellite altitude and stored in a lookup table. When comparing the theoretical pitch angle distributions with the measured particle fluxes, the procedure is as follows: We calculate the ratio between the fluxes detected by the 0° and 90° detector. We apply the telescope's viewing directions relative to the magnetic field and calculate the corresponding ratio for the theoretical solution. Next, we determine which of the theoretical pitch angle distributions best corresponds to the observed ratio. Finally, the size of the BLC, predicted based on the International Geomagnetic Reference Field (IGRF) model, are applied to estimate the precipitating fluxes. The BLC flux estimate is done separately for each energy channel as the level of particle diffusion will vary with energy. A detailed explanation of the method can be found in Nesse Tyssøy et al. (2016).

We used six different satellites during the investigation period; NOAA15, NOAA16, NOAA17, NOAA18, NOAA19, and MetOp-2, as seen in the right panel of Figure 1. The satellites have good coverage in most of the MLT sectors. We bin daily resolved fluxes into eight MLT sectors with 3 hr resolution and 1° magnetic latitude. However, in the Northern Hemisphere (NH), there is insufficient data in sectors 18–21 in the first half of the 11 years and sectors 21–24 in the second half (as seen in the left panel of Figure 1). Hence, we chose to ignore the MLT sectors 18–24.

For each day of the 11-year data series, the near-Earth solar wind condition is classified into three categories: CME, HSS/CIR, and slow ambient solar wind, based on the list created by Ian Richardson of the University

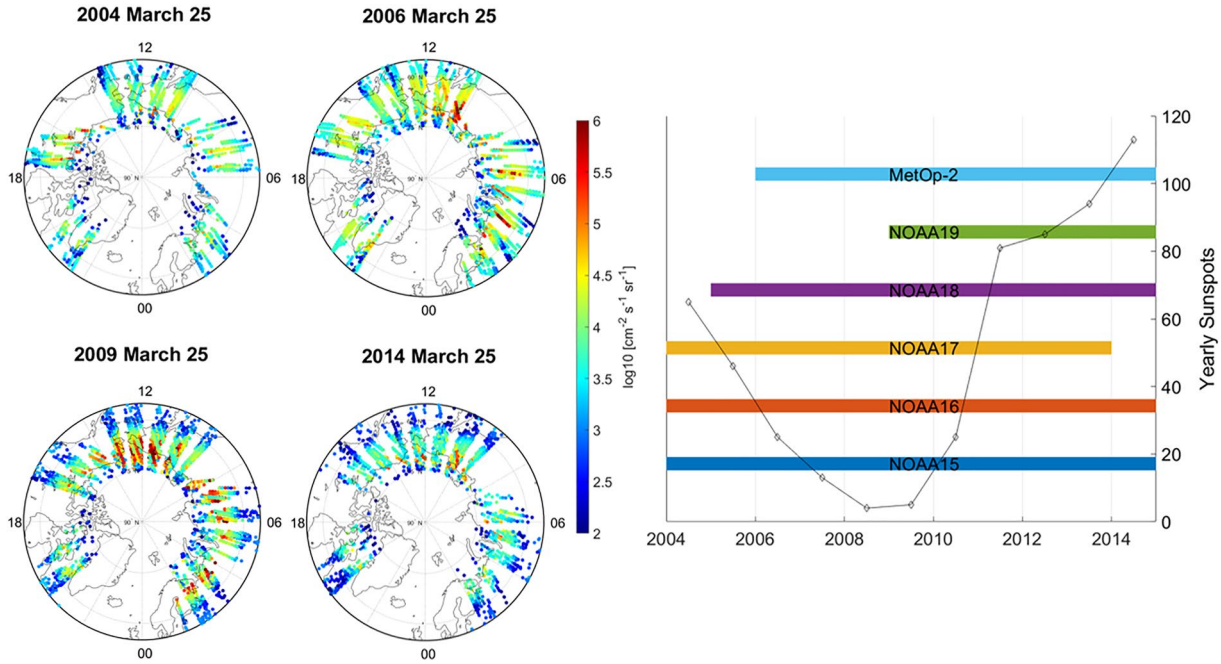

Figure 1. (left) Daily electron flux observation (>43 keV) and satellite ground-track during 25 March 2004, 2006, 2009, and 2014. (right) Polar Orbiting Environmental Satellites and Meteorological Operational satellite coverage during the 11 years of this study.

of Maryland and NASA Goddard Space Flight Center. The classification is done through examination of solar wind plasma parameters and geomagnetic indices obtained from the NASA Omniweb database along with 0.1–100 MeV energetic particle observations and cosmic ray observations from Goddard Space Flight Center instruments (Richardson & Cane, 2012). CIR and ambient will be used in this paper for convenience to denote the HSS/CIR and slow solar wind, respectively.

3. Identifying the Latitude Boundary

In this study, we focus on the NH applying the estimated BLC fluxes over the geomagnetic latitude band from 45° to 75°. We identify the latitude boundaries by first defining a threshold level in the region 50°–60° geomagnetic latitude. We define a threshold value for each channel across all MLT sectors based on mean flux values plus two standard deviation during ambient solar wind conditions.

The equatorward boundary is identified as the geomagnetic latitude at which the fluxes cross this threshold with a positive gradient, as indicated by the blue arrow in the left panel of Figure 2. However, we observe days with enhanced flux in the lower latitude region during modest to strong geomagnetic storm activity causing more than one threshold crossing moving from the equator to the poles, as illustrated by the black box on the right panel of Figure 2. These occurrences have been identified in Kavanagh et al. (2018) as slot region filling events; periods in which MEE penetrate and fill the slot region between the inner and outer radiation belts. These fluxes typically show a slow decay which appears independent of the strongly varying solar wind properties and geomagnetic activity. In such instances, the next positive gradient threshold crossing moving from the equator toward the poles is identified as the equatorward boundary. This will give a systematic lower EEP flux over the hemisphere compared to observations, but justified as the fluxes ignored are precipitated at relatively low latitudes where more efficient photo-chemistry likely renders their chemical imprint insignificant.

We fit a smoothing spline to the data and identify the local maxima and minima. Using these reference points, an algorithm identifies the threshold crossings for days with and without slot filling events for all MLTs and energy channels from 2004 to 2014. The algorithm successfully identified equatorward boundaries from 85% (E1 MLT 0–3) to 94% (E3 MLT 9–12) of the total number of days in the study. As the slot region filling has a slow decay, as seen inside the gray boxes in the 4th panel of Figure 3, there are 489 days for E1 where it was difficult to separate the dynamic boundary from the slot region filling events. We define these days as ambiguous and they

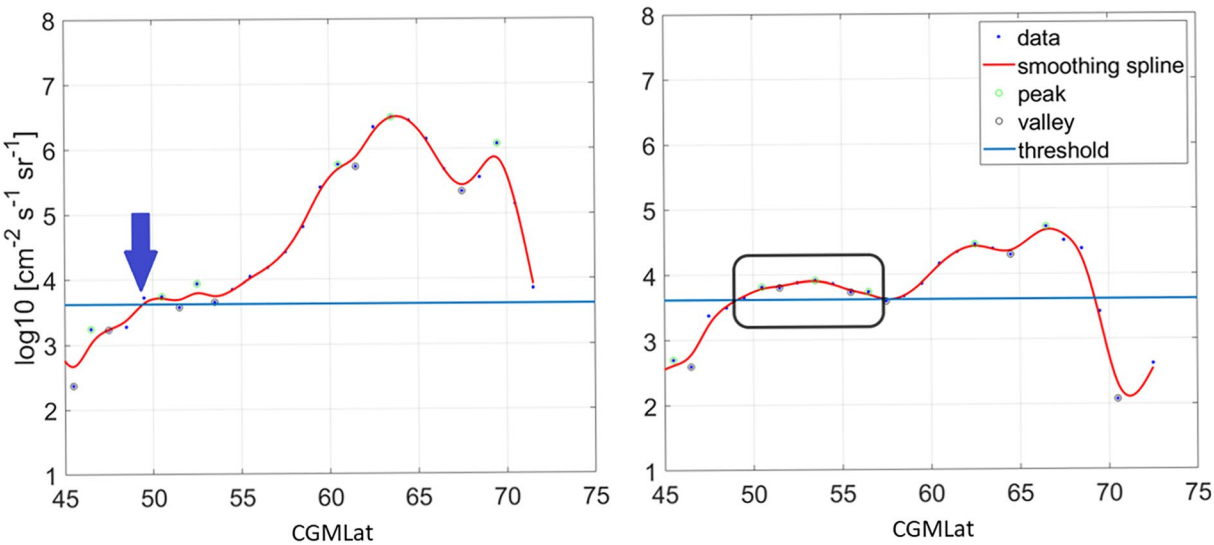

Figure 2. (left) Sample daily flux with one peak above the threshold. (right) Sample daily flux with a double peak above the threshold.

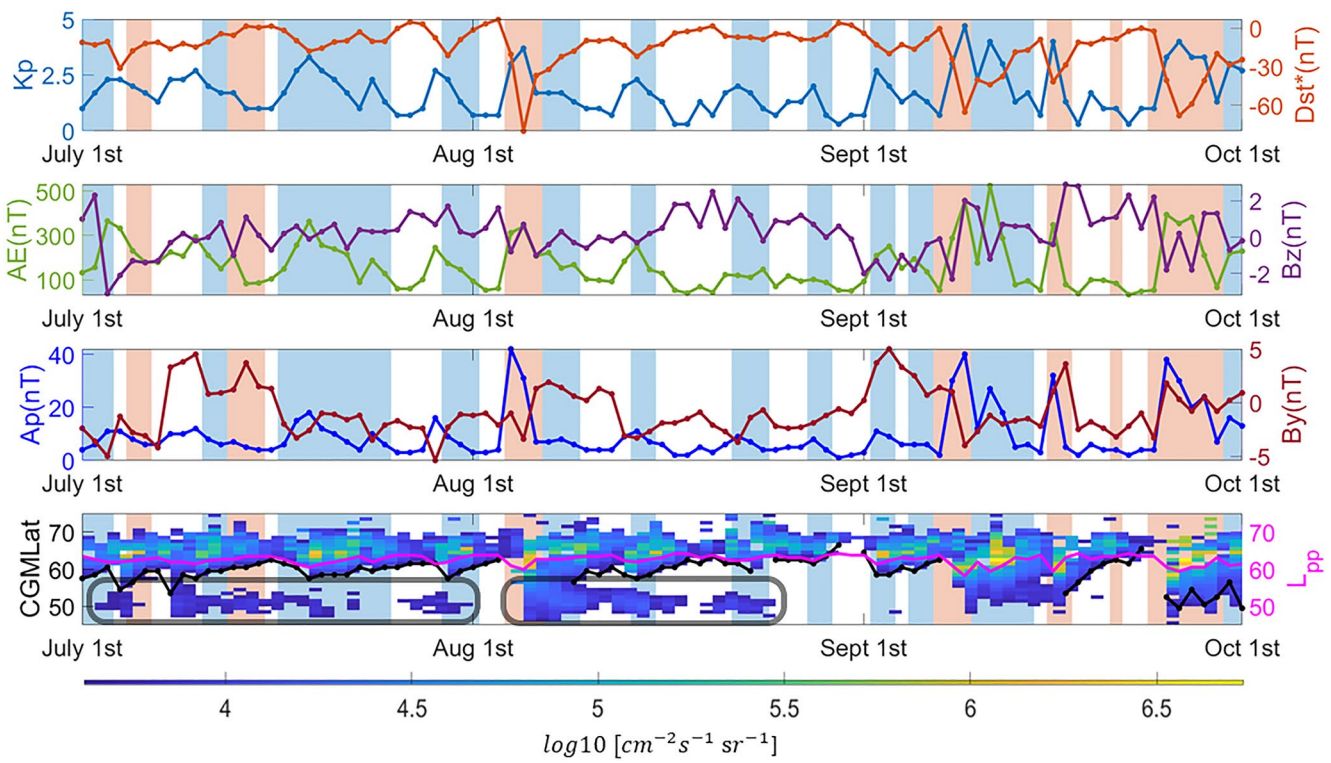

Figure 3. Geomagnetic indices and fluxes above the threshold from July–October 2011. Light red bars represent days with Coronal Mass Ejections, light blue bars days with Co-rotating Interaction Regions, and white bars are days with ambient wind conditions. (1st Panel) Kp on the left *y* axis and pressure corrected Dst (Burton et al., 1975) on the right. (2nd Panel) AE on the left *y* axis and Bz on the right. (3rd Panel) Ap on the left *y* axis and By on the right. (4th Panel) Equatorward boundary identified from the algorithm (black line with dots). The color-plot is fluxes above the threshold for E1 energy channel. The magenta line is the location of plasmapause from (Moldwin et al., 2002) plasmapause model. The gray boxes are slot filling events.

Table 1
Day of Year (DOY) With Ambiguous Boundaries Following the Slot Region Filling Events

2004	2005	2006	2007	2010	2011	2012	2013
1–31	8–25	95–113	29	95–105	76	68–80	145–160
42–48	38–43	127–128	143–149	150–156	149–153	114–122	180–202
70–77	49–51	158–161	184	215–219	156–158	164–166	
95–104	66–73	208–209	192		218–221	169–173	
167	95–110	232–236	344		252–260	191–205	
199	128–179	247–248			298–300	275–277	
200	191–229	334–336				282–295	
205–226	237–264	346–359					
259–268							
314–320							

are not included in the study. Table 1 lists the day of the year (DOY) which are excluded from the analysis, which accounts for 12% of the total days in the study.

4. Predicting the Latitude Boundary

To develop a solar wind parameter or geomagnetic index-based model to predict the equatorward boundaries of MEE precipitation, the parameter that correlates best with the identified boundaries needs to be determined. The parameters considered are pressure-corrected Dst, Kp, AE, Ap, Bz, By, Ey, solar wind flow pressure (P), and solar wind flow speed (v). The pressure-corrected Dst index, Dst*, removes the contribution from the current induced in the magnetopause from the solar wind dynamic pressure. Therefore, Dst* is a better representation of the ring current (Burton et al., 1975):

$$Dst^{*} = Dst - \left(15.8 \times P^{0.5}\right) + 20 \quad (1)$$

Dst* shows the highest Pearson correlation coefficient with the equatorward boundaries of >43 keV MEE precipitation with a value of 0.77. Kp and AE have correlation coefficients of 0.66 and 0.65, respectively. Figure 4 shows the associated scatter plots for the boundaries and Dst*, Kp, and AE. In general, low boundaries (<~53°) appear to be associated with a wide range of Dst*, Kp, and AE values which might suggest that there are still a few data points associated with the slot region filling events discussed in Section 3. Nevertheless, both the Dst* and AE index have a well-defined upper envelope which clearly moves to lower latitudes as the geomagnetic activity increases. Furthermore, the 90/10 percentile lines in the scatter plots show that Kp has a higher spread of the predicted latitudes of ~2.74/2.75 compared to AE ~2.67/2.64 and Dst* ~ 2.25/2.23. Dst* maintains the best

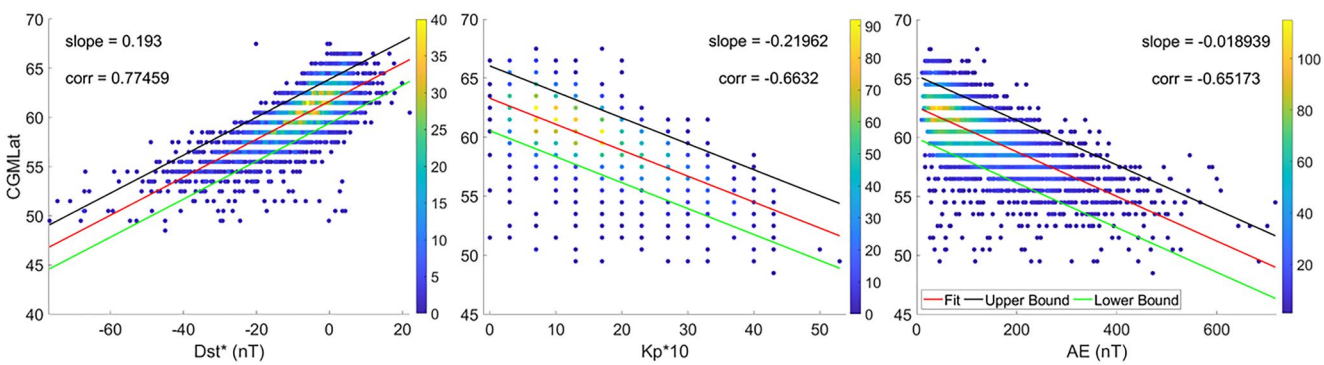

Figure 4. A comparison of the three best correlated indices with the identified boundary. (left) Dst, (center) Kp, and (right) AE. The red line is the linear fit. The green and the black lines are the 10th and the 90th percentiles of the residuals, respectively, when the boundaries predicted by each index is subtracted from the identified boundaries. The color bar represents the number density of data points. The data are from the E1 (>43 keV) energy channel in the Magnetic Local Time sector 0–3.

Table 2
Pearson Correlation Coefficients Between the Equatorward Boundaries and Dst, Kp, and AE*

	E1	E2	E3
Dst* correlation coefficient	**0.77**	**0.72**	**0.52**
Dst* 90th percentile (CGMLat)	2.25	2.24	2.11
Dst* 10th percentile (CGMLat)	−2.23	−2.10	−1.91
Kp correlation coefficient	**0.66**	**0.56**	**0.36**
Kp 90th percentile (CGMLat)	2.74	2.51	2.20
Kp 10th percentile (CGMLat)	−2.75	−2.57	−2.05
AE correlation coefficient	**0.65**	**0.56**	**0.37**
AE 90th percentile (CGMLat)	2.67	2.56	2.24
AE 10th percentile (CGMLat)	−2.64	−2.40	−2.04

Note. The 90th and 10th percentiles are the residuals when the boundaries predicted by each index is subtracted from the identified boundaries for E1, E2, and E3. The bold values indicates the most important values in this table.

correlation coefficient values for the E2 and E3 energy channels, as seen in Table 2. Therefore, the Dst* is selected as the best predictor for the equatorward boundary variability.

A linear model for the boundaries is found by fitting least squares regression on Dst* and using the following equation to calculate the boundaries for each of the MLT regions and energy channels separately:

$$Model\ Boundary = \text{y-intercept} + (Regression\ Coefficient \times Dst^{*}) \quad (2)$$

The *y*-intercepts and Pearson correlation coefficients for the three energy channels and six MLT sectors corresponding to Dst* model are listed in Table 3. Figure 5 shows a comparison between the identified and modeled boundaries for each energy channel in the MLT regions 0–3. The model (red dotted line) closely follows the identified boundaries (black dotted line) for all energy channels. As evident from Table 3, there is less variability in the equatorward boundary in the higher energy channels E2 and E3 compared to E1. The empty patches are days from Table 1 that are excluded from this study. Nevertheless, there appears to be a tendency to underestimate the equatorward boundary position in the aftermath of a slot region filling event. Furthermore, the model overestimates the equatorward boundary position in periods of weak activity.

5. Accuracy of the Dst* Model

To systematically explore the performance of the Dst* model, a residual analysis on the difference between the identified and Dst-regressed boundary is performed:

$$Residual\ Boundary = Identified\ Boundary - Model\ Boundary \quad (3)$$

The 3rd panel in Figure 6 shows the residual boundary plot for the E1 energy channel. Eighty percent of the residuals falls within ±2.2° cgmlat. However, the residuals do exhibit a solar cycle bias. The average error is −1.84° cgmlat during the declining phase in 2004, 1.51° cgmlat during the solar minimum year 2009, and 0.18° cgmlat near solar maximum in 2014, causing a potential solar cycle bias of up to 3.35° cgmlat. This systematic bias potentially arises because the quiet time baseline of the Dst index varies with the solar cycle. The Dst index will therefore underestimate or overestimate magnetic activity as a function of the solar cycle (Temerin & Li, 2015).

Considering the solar wind drivers, 12% of the total number of days in the study are dominated by CMEs, 40% of the days are characterized as CIRs, and 48% are described as ambient solar wind conditions. The Dst* model has the best predictability during CIRs as seen in Figure 7. This can also be seen in the 4th panel of Figure 6 where the CIR-dominated period from late 2006 to late 2008 period gives the smallest residuals. The dependency of the solar wind driver might be part of the systematic bias throughout the solar cycle. The frequency of CMEs peaks during solar maximum, HSSs/CIRs are more common in the declining phase, while ambient solar

Table 3
y-Intercepts, Regression Coefficients, and Correlation Coefficients for All Energy Channels and Magnetic Local Time (MLT) Sectors

	E1	E2	E3
MLT 0_3	61.65 + 0.1930Dst*; R = **0.7746**	60.55 + 0.1499Dst*; R = **0.7187**	59.60 + 0.0811Dst*; R = **0.5222**
MLT 3_6	61.76 + 0.1869Dst*; R = **0.7893**	60.62 + 0.1472Dst*; R = **0.7163**	59.48 + 0.1097Dst*; R = **0.6453**
MLT 6_9	61.94 + 0.1709Dst*; R = **0.7239**	60.78 + 0.1326Dst*; R = **0.6581**	59.67 + 0.1077Dst*; R = **0.6297**
MLT 9_12	61.66 + 0.1895Dst*; R = **0.7413**	60.62 + 0.1484; R = **0.6881**	59.54 + 0.1140Dst*; R = **0.6389**
MLT 12_15	61.98 + 0.2008Dst*; R = **0.7475**	60.67 + 0.1517Dst*; R = **0.6838**	59.53 + 0.1201Dst*; R = **0.6457**
MLT 15_18	61.91 + 0.1940Dst*; R = **0.7218**	60.51 + 0.1455Dst*; R = **0.6522**	59.38 + 0.1172Dst*; R = **0.6226**

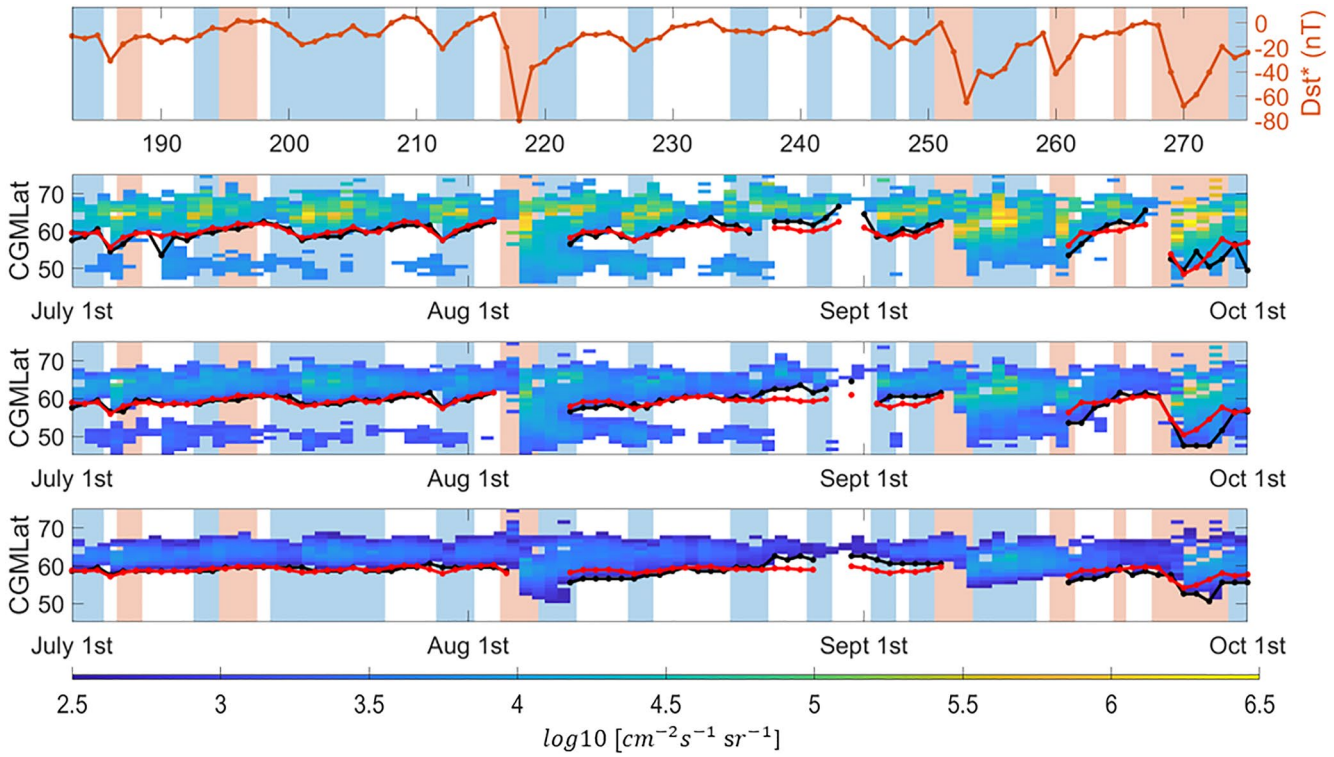

Figure 5. Identified boundaries and modeled boundaries for the E1, E2, and E3 energy channels from July to October 2011. Light red bars represent days with Coronal Mass Ejections, light blue bars days with Co-rotating Interaction Regions, and white bars are days with ambient wind conditions. (1st Panel) Dst index. Equatorward boundary identified from the algorithm (black dotted line) and the modeled equatorward boundary (red dotted line) for energy channels: (2nd Panel) E1, (3rd Panel) E2, and (4th Panel) E3. The color plots are fluxes above the threshold.

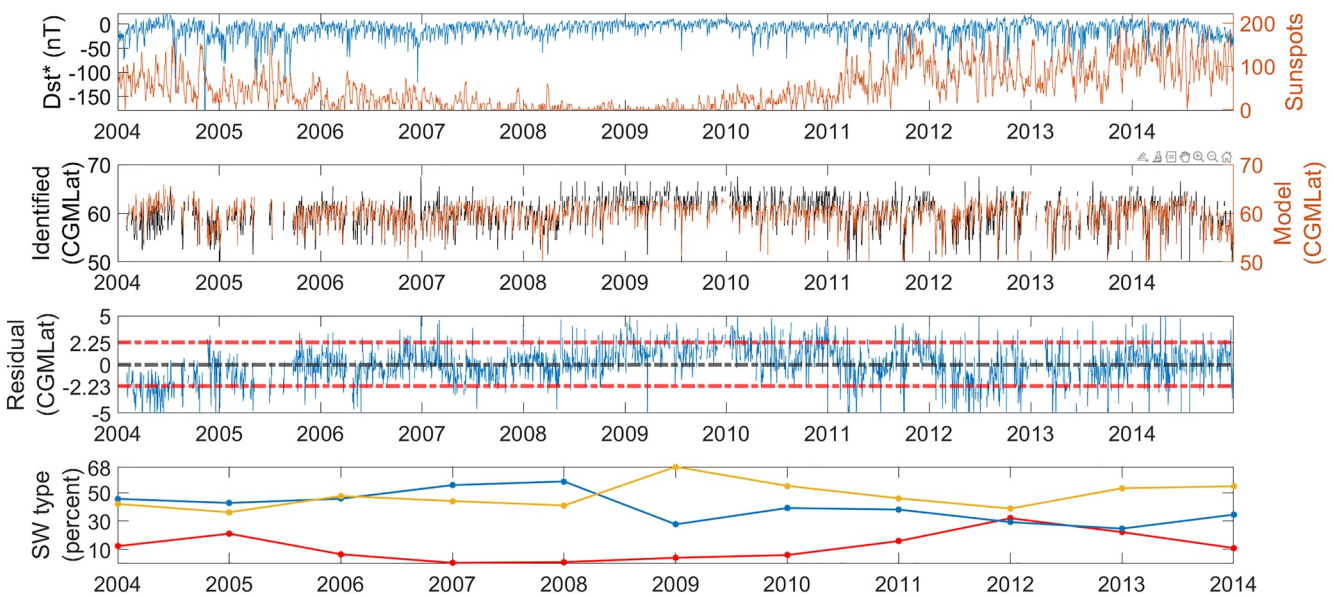

Figure 6. (1st Panel) Dst* (blue) and daily sunspot numbers (red) from 2004 to 2014. (2nd Panel) Identified boundaries (black) and Modeled boundaries (red). (3rd Panel) Residual plot. The red dashed line above and below the 0-line in the 3rd panel represents the 90th percentile value. (4th Panel) Percentage of each solar wind driver for each year in the study. Red line represents Coronal Mass Ejections, blue line Co-rotating Interaction Regions, and yellow line ambient solar wind conditions. The boundaries and residuals are for the E1 energy channel in the Magnetic Local Time sector 0–3 across the 11 years of this study.

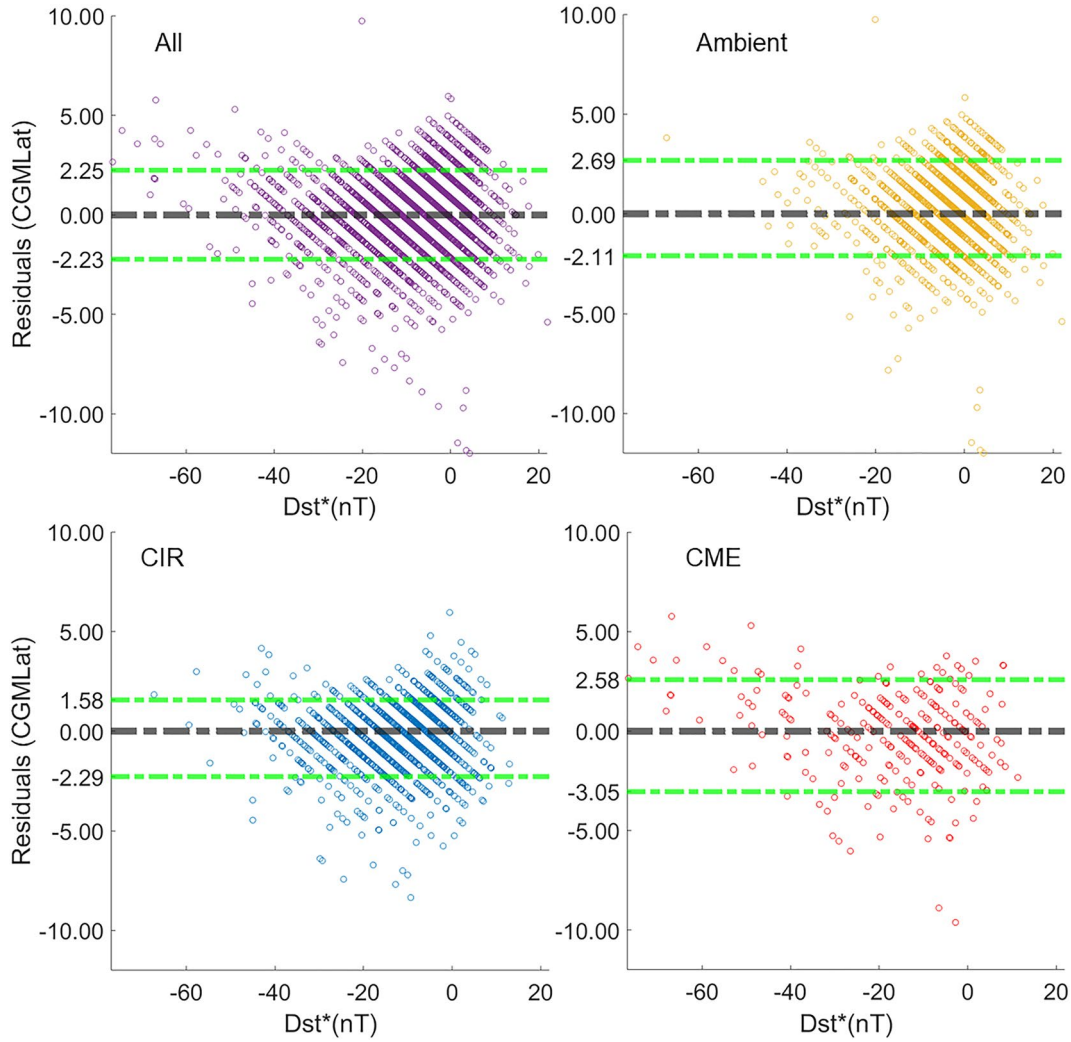

Figure 7. A comparison of the accuracy of the Dst* model for different solar wind drivers. (top left) Residuals for all solar wind drivers. (top right) Residuals for days with ambient solar wind conditions. (bottom left) Residuals for days with Co-rotating Interaction Regions. (bottom right) Residuals for days with Coronal Mass Ejections. The green dashed line above and below the black 0-line are the 90 and 10 percentiles of the residuals, respectively.

Table 4
The Difference Between Identified and Dst Model Boundaries in CGMLat for the Six Investigated Magnetic Local Time (MLT) Sectors and the Three Energy Channels*

	E1	E2	E3
MLT 0–3	2.25, −2.23	2.24, −2.10	2.11, −1.91
MLT 3–6	2.25, −2.22	2.28, −2.22	2.51, −2.51
MLT 6–9	2.47, −2.45	2.38, −2.21	2.52, −2.50
MLT 9–12	2.66, −2.64	2.51, −2.32	2.53, −2.53
MLT 12–15	2.78, −2.67	2.59, −2.34	2.62, −2.57
MLT 15–18	2.79, −2.79	2.58, −2.45	2.69, −2.71

Note. The numbers are the 90th and the 10th percentiles of the residuals.

wind dominates the solar minimum (Richardson et al., 2001). Therefore, as a future effort we will investigate if a model with solar wind drivers as a dependent variable can potentially reduce the solar cycle bias. It is also worth considering different geomagnetic indices and solar wind parameters during different phases of the solar cycle as they might be better at predicting MEE precipitation for different solar wind drivers (Borovsky & Denton, 2006).

Exploring the MLT dependence of the Dst* model, the midnight sector MLT 0–3 was found to have the best predictability, and the afternoon sector MLT 15–18 the highest uncertainty in all energy channels. The relatively highest uncertainty in the afternoon sector could be related to the Relativistic Electron Precipitation (REP) occurring in the MLT sector 14–20. These events have been shown by Smith et al. (2016) to be correlated with multiple solar wind parameters and geomagnetic indices, tying them to EMIC-driven precipitation. Table 4 shows the 90th and 10th percentiles of residuals for all MLT sectors and energy channels used in this study.

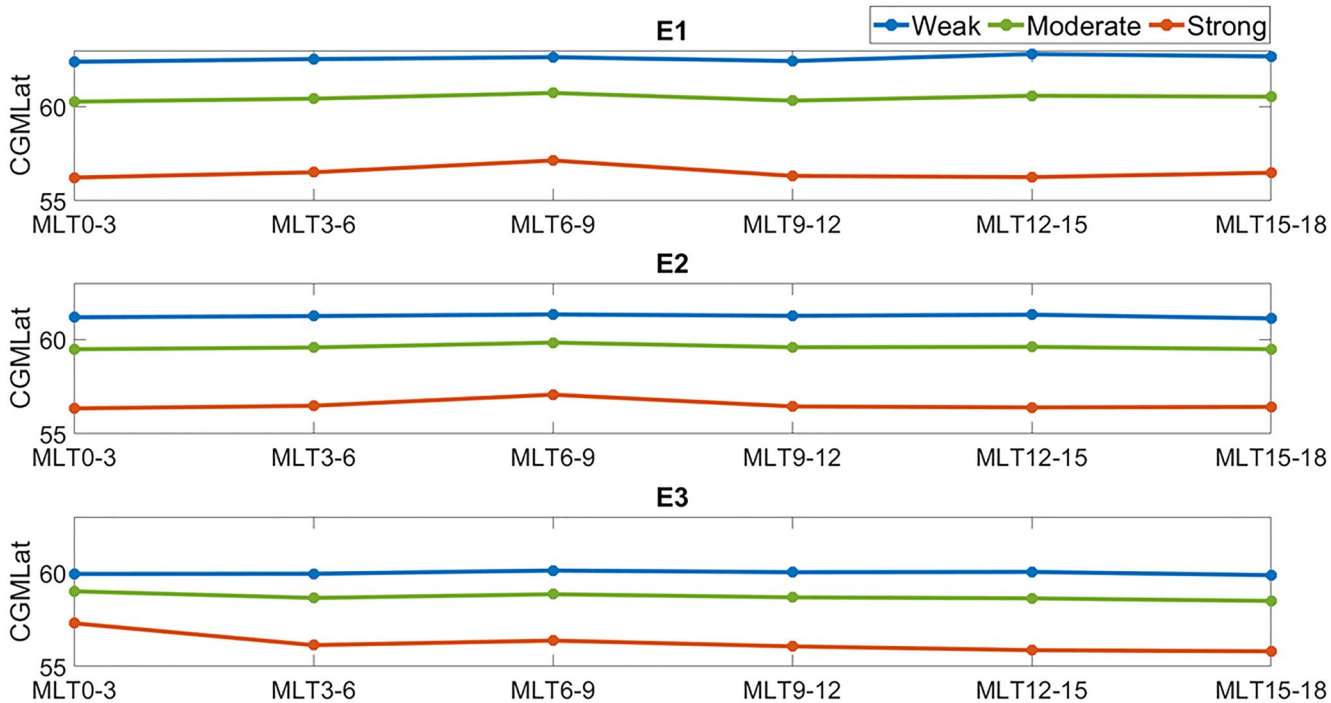

Figure 8. Variation of the median boundary of the Dst* model in each Magnetic Local Time sector and each energy channel for different geomagnetic activity levels.

The variability of the median boundary with respect to MLT and energy for different levels of geomagnetic activity is also investigated (Figure 8). All geomagnetic activity above the 80th percentile of the average Dst (0.89 nT) are defined as weak, while activity below the 20th percentile (−20.65 nT) are considered strong. Everything in between is categorized as a moderate activity. With increasing strength of Dst*, the boundaries are pushed equatorward as expected for all three energy channels. The E1 channel is the most dynamic of the three and exhibits the most poleward boundary, followed by E2, and lastly E3. Nevertheless, no systematic variation of the MEE precipitating boundaries as a function of MLT is observed for the same level of geomagnetic activity consistent with Table 4. The weak MLT dependency might be due to that MEE will travel multiple times around the Earth before being lost to the atmosphere. By using daily resolved MEE fluxes, the MLT variability associated with for example, isolated substorms will be averaged out. Hence, a higher temporal resolution might be needed to observe any notable MLT dependency for the precipitating latitudes.

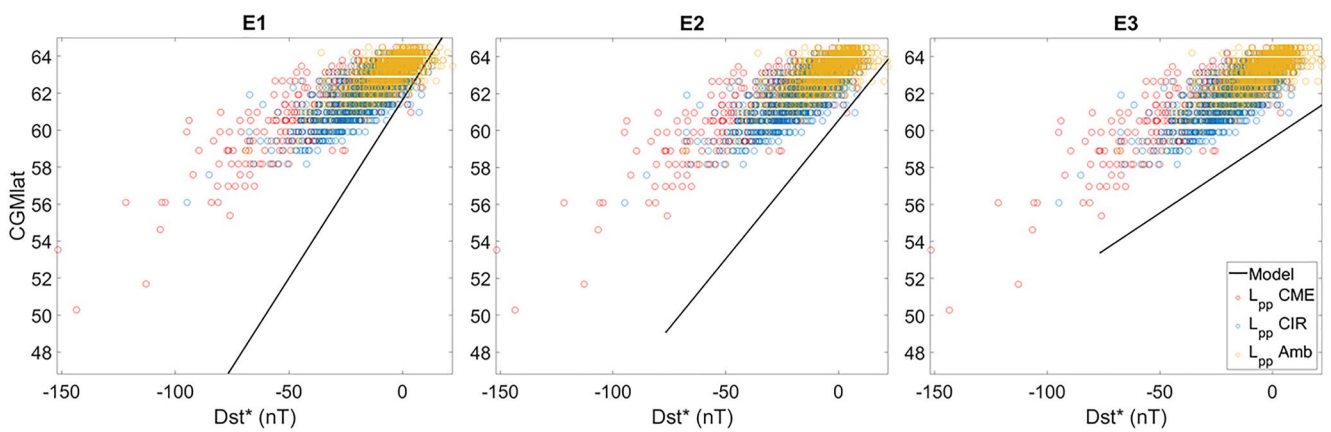

Figure 9. Location of the plasmapause estimated from Moldwin et al. (2002)'s plasmapause model are scatter-plotted for different solar wind drivers (red for Coronal Mass Ejection, blue for Co-rotating Interaction Region, and yellow for ambient). The equatorward boundaries predicted by the Dst* model is the black line. The data are for E1, E2, and E3 energy channels from left to right, respectively.

A comparison of the Dst* model with Moldwin et al. (2002)'s plasmapause model for the E1, E2, and E3 channels is presented in Figure 9. The solid black line represents the equatorward boundary predicted by the Dst* model. The red, blue, and yellow scatterplots depict the location of the plasmapause during CME, CIR, and ambient solar wind conditions. For the E1 channel, the more negative the Dst* index becomes, the larger the deviation is between the location of the plasmapause with respect to the Dst* model. Hence, the largest discrepancies are naturally found predominantly during days with CMEs. The location of the plasmapause is the closest to the Dst* model during ambient solar wind conditions compared to CIRs and CMEs. The differences between the plasmapause model and the Dst* model is less prominent in the E3-channel as the equatorward boundary is not as dynamic compared to the E1-channel, as shown in the 4th panel of Figure 5. Therefore, the location of the plasmapause in E3 is closer to the equatorward boundary than in E1, and appears to have a similar dependency on Dst*.

van de Kamp et al. (2016) and van de Kamp et al. (2018) use Moldwin et al. (2002)'s plasmapause model dependent on Ap, to predict the equatorward boundary of the >30 keV electron flux. Furthermore, van de Kamp et al. (2018) models the precipitation as a function of MLT. van de Kamp et al. (2018) finds a dependence of MEE flux on MLT in agreement with previous studies such as Wissing et al. (2008), Meredith et al. (2011), and Ødegaard et al. (2017). However, since Moldwin et al. (2002)'s plasmapause model is independent of MLT, the variation of precipitation boundaries with geomagnetic activity remains almost the same across all MLT sectors. This is consistent with Figure 8. Moreover, the equatorward boundaries predicted by Dst* model predicts are energy dependent, where the equatorward extent of the precipitation is pushed toward lower latitudes for higher electron energies. Therefore, based on Figure 9, it is likely that the discrepancy between the precipitation region in van de Kamp et al. (2016) and the Dst* model will increase with higher activity for E1, but have a more consistent discrepancy for the higher energies E2 and E3. We also note that the MLT sectors 18–21 and 21–24 are omitted in this study because of insufficient data.

In the HEPPA III intercomparison study in Nesse Tyssøy et al. (2022), a comparison of the latitudinal extent of the MEE precipitation region is done for eight different ionization rate estimates including the van de Kamp et al. (2016) model and the BLC rates used here. For the respective period, the van de Kamp et al. (2016) and plasmapause model provide the most prudent estimate of the equatorward boundary compared to the other ionization rate estimates. In particular, the ionization rates based on both the 0° and 90° telescopes, such as the BLC fluxes shown here, predict a much larger extent of the equatorward boundaries, and will hence lead to a stronger chemical impact.

6. Conclusion

This study investigates the variation of equatorward boundary of precipitating MEE electrons with respect to different geomagnetic indices and solar wind parameters. BLC measurements of >43, >114, and >292 keV MEE fluxes from MEPED detectors from 2004 to 2014 are used to develop a geomagnetic index-based model. This model is capable of predicting the equatorward extend of MEE precipitation in the NH over the geomagnetic latitude band of 45°–75°. An algorithm based on a threshold level identifies boundaries for the E1(>43 keV), E2(>114 keV), and E3(>292 keV) energy channels for MLT sectors 0–3, 3–6, 6–9, 9–12, 12–15, and 15–18. We find Dst* to be the best predictor of the identified boundaries compared to Kp, AE, Ap, Bz, By, Ey, solar wind flow pressure (P), and solar wind flow speed (v). The model uses a linear regression of Dst* to estimate equatorward boundaries with an error estimate of ±2.2° cgmlat. The model has a solar cycle bias from underestimation and overestimation of magnetic activity as a function of the solar cycle. The model also exhibits a bias based on solar wind drivers thus exacerbating the Dst* bias. The equatorward boundaries are pushed to lower latitudes with an increase in strength of the geomagnetic activity. However, no significant change in the median boundary as function of MLT is observed for the same level of geomagnetic activity. The more negative the Dst* index becomes, the larger the E1 boundaries deviate from Moldwin et al. (2002)'s plasmapause model and to a greater extent for CME and CIR events compared to ambient days.

In future work, we will explore to which degree the type of solar wind driver as a dependent variable, can improve the accuracy of a geomagnetic index based model. Furthermore, the choice to exclude the slot filling events implies a systematic underestimation of the hemispheric electron energy input at mid and low geomagnetic latitudes. This will be quantified in a future study, alongside an assessment of the chemical imprint considering the geographic latitudes and level of photolysis. Alongside predictions of the intensity of the MEE fluxes (Tyssoy, 2021), the Dst* model will be a key element for constructing a realistic estimate of EEP variability to be applied in atmosphere climate models. Moreover, the model can also be applied to examine the importance of the location of the plasmapause in moderating wave-particle interactions that lead to precipitation and how the precipitation boundaries might relate to the inner edge of the outer radiation belts.

Data Availability Statement

The NOAA/POES MEPED data used in this study are available from the National Oceanic and Atmospheric Administration (https://www.ngdc.noaa.gov/stp/satellite/poes/dataaccess.html). The MLT and CGMLat sorted MEPED data are available at Zenodo via https://doi.org/10.5281/zenodo.6590387. Geomagnetic indices and solar wind parameters were obtained from NASA Omniweb at https://omniweb.gsfc.nasa.gov/form/dx1.html.

Acknowledgments
The study is supported by the Norwegian Research Council (NRC) under contract nos. 223252 and 302040. HNT further acknowledge the Young CAS (Centre for Advanced Studies) fellow program. IGR acknowledges support from the ACE mission. The authors thank the Space Weather Prediction Center (SWPC), NOAA for providing the MEPED data.

References

Andersson, M. E., Verronen, P. T., Wang, S., Rodger, C. J., Clilverd, M. A., & Carson, B. R. (2012). *Precipitating radiation belt electrons and enhancements of mesospheric hydroxyl during 2004–2009* (Vol. 117). Blackwell Publishing Limited. https://doi.org/10.1029/2011JD017246

Baumgaertner, A. J., Seppälä, A., Jöckel, P., & Clilverd, M. A. (2011). Geomagnetic activity related NO_x enhancements and polar surface air temperature variability in a chemistry climate model: Modulation of the NAM index. *Atmospheric Chemistry and Physics*, *11*(9), 4521–4531. https://doi.org/10.5194/acp-11-4521-2011

Borovsky, J. E., & Denton, M. H. (2006). Differences between CME-driven storms and CIR-driven storms. *Journal of Geophysical Research*, *111*(A7), A07S08. https://doi.org/10.1029/2005JA011447

Burton, R., McPherron, R., & Russell, C. (1975). An empirical relationship between interplanetary conditions and Dst. *Journal of Geophysical Research*, *80*(31), 4204–4214. https://doi.org/10.1029/JA080i031p04204

Carson, B. R., Rodger, C. J., & Clilverd, M. A. (2013). POES satellite observations of EMIC-wave driven relativistic electron precipitation during 1998–2010. *Journal of Geophysical Research: Space Physics*, *118*(1), 232–243. https://doi.org/10.1029/2012JA017998

Damiani, A., Funke, B., López-Puertas, M., Santee, M. L., Cordero, R. R., & Watanabe, S. (2016). Energetic particle precipitation: A major driver of the ozone budget in the Antarctic upper stratosphere. *Geophysical Research Letters*, *43*(7), 3554–3562. https://doi.org/10.1002/2016GL068279

Evans, D., & Greer, M. (2000). *Polar orbiting environmental satellite space environment monitor-2: Instrument description and archive data documentation*. U.S. Department of Commerce, National Oceanic and Atmospheric Administration, Oceanic and Atmospheric Research Laboratories, Space Environment Center.

Friedel, R., Reeves, G., & Obara, T. (2002). Relativistic electron dynamics in the inner magnetosphere—A review. *Journal of Atmospheric and Solar-Terrestrial Physics*, *64*(2), 265–282. https://doi.org/10.1016/S1364-6826(01)00088-8

Gasque, L. C., Millan, R. M., & Shekhar, S. (2021). Statistically determining the spatial extent of relativistic electron precipitation events using 2-s polar-orbiting satellite data. *Journal of Geophysical Research: Space Physics*, *126*(4), e2020JA028675. https://doi.org/10.1029/2020JA028675

Hardman, R., Clilverd, M. A., Rodger, C. J., Brundell, J. B., Duthie, R., Holzworth, R. H., et al. (2015). A case study of electron precipitation fluxes due to plasmaspheric hiss. *Journal of Geophysical Research: Space Physics*, *120*(8), 6736–6748. https://doi.org/10.1002/2015JA021429

Kavanagh, A. J., Cobbett, N., & Kirsch, P. (2018). Radiation belt slot region filling events: Sustained energetic precipitation into the mesosphere. *Journal of Geophysical Research: Space Physics*, *123*(9), 7999–8020. https://doi.org/10.1029/2018JA025890

Kennel, C. F., & Petschek, H. E. (1966). Limit on stably trapped particle fluxes. *Journal of Geophysical Research*, *71*, 1–28.

Maliniemi, V., Asikainen, T., Salminen, A., & Mursula, K. (2019). Assessing North Atlantic winter climate response to geomagnetic activity and solar irradiance variability. *Quarterly Journal of the Royal Meteorological Society*, *145*(725), 3780–3789. https://doi.org/10.1002/qj.3657

Maliniemi, V., Nesse Tyssøy, H., Smith-Johnsen, C., Arsenovic, P., & Marsh, D. R. (2021). Effects of enhanced downwelling of NO_x on Antarctic upper-stratospheric ozone in the 21st century. *Atmospheric Chemistry and Physics*, *21*(14), 11041–11052. https://doi.org/10.5194/acp-21-11041-2021

Meredith, N. P., Horne, R. B., Lam, M. M., Denton, M. H., Borovsky, J. E., & Green, J. C. (2011). Energetic electron precipitation during high-speed solar wind stream driven storms. *Journal of Geophysical Research: Space Physics*, *116*(5), A05223. https://doi.org/10.1029/2010JA016293

Millan, R., & Thorne, R. (2007). Review of radiation belt relativistic electron losses. *Journal of Atmospheric and Solar-Terrestrial Physics*, *69*(3), 362–377. https://doi.org/10.1016/j.jastp.2006.06.019

Moldwin, M. B., Downward, L., Rassoul, H., Amin, R., & Anderson, R. (2002). A new model of the location of the plasmapause: CRRES results. *Journal of Geophysical Research*, *107*(A11), 1339. https://doi.org/10.1029/2001JA009211

Nesse Tyssøy, H., Sandanger, M. I., Ødegaard, L. K., Stadsnes, J., Aasnes, A., & Zawedde, A. E. (2016). Energetic electron precipitation into the middle atmosphere—Constructing the loss cone fluxes from MEPED POES. *Journal of Geophysical Research A: Space Physics*, *121*(6), 5693–5707. https://doi.org/10.1002/2016JA022752

Nesse Tyssøy, H., Sinnhuber, M., Asikainen, T., Bender, S., Clilverd, M. A., Funke, B., et al. (2022). HEPPA III intercomparison experiment on electron precipitation impacts: 1. Estimated ionization rates during a geomagnetic active period in April 2010. *Journal of Geophysical Research: Space Physics*, *127*(1), e2021JA029466. https://doi.org/10.1029/2021JA029128

Ødegaard, L.-K. G., Nesse, T. H., Sandanger, J., Stadsnes, M. I., & Søraas, F. (2016). Space Weather impact on the degradation of NOAA POES MEPED proton detectors. *Journal of Space Weather and Space Climate*, *6*, A26. https://doi.org/10.1051/swsc/2016020

Ødegaard, L.-K. G., Nesse, T. H., Søraas, F., Stadsnes, J., & Sandanger, M. I. (2017). Energetic electron precipitation in weak to moderate corotating interaction region-driven storms. *Journal of Geophysical Research: Space Physics*, *122*(3), 2900–2921. https://doi.org/10.1002/2016JA023096

Pierrard, V., Botek, E., Ripoll, J. F., Thaller, S. A., Moldwin, M. B., Ruohoniemi, M., & Reeves, G. (2021). Links of the plasmapause with other boundary layers of the magnetosphere: Ionospheric convection, radiation belt boundaries. *Auroral Oval Frontiers in Astronomy and Space Sciences*, *8*, 728531. https://doi.org/10.3389/fspas.2021.728531

Richardson, I. G. (2018). *Solar wind stream interaction regions throughout the heliosphere* (Vol. 15). Springer International Publishing. https://doi.org/10.1007/s41116-017-0011-z

Richardson, I. G., & Cane, H. V. (2012). Near-earth solar wind flows and related geomagnetic activity during more than four solar cycles (1963–2011). *Journal of Space Weather and Space Climate*, *2*, A02. https://doi.org/10.1051/swsc/2012003

Richardson, I. G., Cliver, E. W., & Cane, H. V. (2001). Sources of geomagnetic storms for solar minimum and maximum conditions during 1972–2000. *Geophysical Research Letters*, *28*(13), 2569–2572. https://doi.org/10.1029/2001GL013052

Rodger, C., Clilverd, M. A., Thomson, N. R., Gamble, R. J., Seppälä, A., Turunen, E., et al. (2007). Radiation belt electron precipitation into the atmosphere: Recovery from a geomagnetic storm. *Journal of Geophysical Research: Space Physics*, *112*(A11), A12304. https://doi.org/10.1029/2007JA012383

Rodger, C. J., Clilverd, M. A., Green, J. C., & Lam, M. M. (2010). Use of POES SEM-2 observations to examine radiation belt dynamics and energetic electron precipitation into the atmosphere. *Journal of Geophysical Research: Space Physics*, *115*(4), A12304. https://doi.org/10.1029/2008JA014023

Sandanger, M., Ødegaard, L., Hn, T., Stadsnes, J., Søraas, F., Oksavik, K., & Aarsnes, K. (2015). In-flight calibration of NOAA POES proton detectors—Derivation of the MEPED correction factors. *Journal of Geophysical Research: Space Physics*, *120*(11), 9578–9593. https://doi.org/10.1002/2015JA021388

Seppälä, A., Randall, C., Clilverd, M., Rozanov, E., & Rodger, C. (2009). Geomagnetic activity and polar surface air temperature variability. *Journal of Geophysical Research: Space Physics*, *114*(A10), A014029. https://doi.org/10.1029/2008JA014029

Shekhar, S., Millan, R., & Smith, D. (2017). A statistical study of the spatial extent of relativistic electron precipitation with polar orbiting environmental satellites. *Journal of Geophysical Research: Space Physics*, *122*(11), 274–311. https://doi.org/10.1002/2017JA024716

Shelley, E. G., Johnson, R. G., & Sharp, R. D. (1972). Satellite observations of energetic heavy ions during a geomagnetic storm. *Journal of Geophysical Research*, *77*(31), 6104–6110. https://doi.org/10.1029/ja077i031p06104

Smith, D. M., Casavant, E. P., Comess, M. D., Liang, X., Bowers, G. S., Selesnick, R. S., et al. (2016). The causes of the hardest electron precipitation events seen with SAMPEX. *Journal of Geophysical Research: Space Physics*, *121*(9), 8600–8613. https://doi.org/10.1002/2016JA022346

Solomon, S., Crutzen, P. J., & Roble, R. G. (1982). Photochemical coupling between the thermosphere and the lower atmosphere: 1. Odd nitrogen from 50 to 120 km. *Journal of Geophysical Research*, *87*(C9), 7206–7220. https://doi.org/10.1029/JC087iC09p07206

Temerin, M., & Li, X. (2015). The Dst index underestimates the solar cycle variation of geomagnetic activity. *Journal of Geophysical Research: Space Physics*, *120*(7), 5603–5607. https://doi.org/10.1002/2015JA021467

Theodoridis, G. C., & Paolini, F. R. (1967). Pitch angle diffusion of relativistic outer belt electrons. *Annales de Geophysique*, *23*, 375–381.

Tyssøy, H. N., Haderlein, A., Sandanger, M., & Stadsnes, J. (2019). Intercomparison of the POES/MEPED loss cone electron fluxes with the CMIP6 parametrization. *Journal of Geophysical Research: Space Physics*, *124*(1), 628–642. https://doi.org/10.1029/2018JA025745

Tyssøy, H. N., Partamies, N., Babu, E. M., Smith-Johnsen, C., & Salice, J. A. (2021). The Predictive Capabilities of the Auroral Electrojet Index for Medium Energy Electron Precipitation. *Frontiers in Astronomy and Space Sciences*, *8*. https://doi.org/10.3389/fspas.2021.714146

Van Allen, J. A. (1959). The geomagnetically trapped corpuscular radiation. *Journal of Geophysical Research*, *64*(11), 1683–1689. https://doi.org/10.1029/JZ064i011p01683

van de Kamp, M., Rodger, C. J., Seppälä, A., Clilverd, M. A., & Verronen, P. T. (2018). An updated model providing long-term data sets of energetic electron precipitation, including zonal dependence. *Journal of Geophysical Research: Atmospheres*, *123*(17), 9891–9915. https://doi.org/10.1029/2017JD028253

van de Kamp, M., Seppälä, A., Clilverd, M. A., Rodger, C. J., Verronen, P. T., & Whittaker, I. C. (2016). A model providing long-term data sets of energetic electron precipitation during geomagnetic storms. *Journal of Geophysical Research*, *121*(20), 12520. https://doi.org/10.1002/2015JD024212

Verronen, P. T., Rodger, C. J., Clilverd, M. A., & Wang, S. (2011). First evidence of mesospheric hydroxyl response to electron precipitation from the radiation belts. *Journal of Geophysical Research*, *116*(7), D07307. https://doi.org/10.1029/2010JD014965

Voss, H., Walt, M., Imhof, W., Mobilia, J., & Inan, U. (1998). Satellite observations of lightning-induced electron precipitation. *Journal of Geophysical Research*, *103*(A6), 11725–11744. https://doi.org/10.1029/97JA02878

Whittaker, I. C., Clilverd, M. A., & Rodger, C. J. (2014). Characteristics of precipitating energetic electron fluxes relative to the plasmapause during geomagnetic storms. *Journal of Geophysical Research: Space Physics*, *119*(11), 8784–8800. https://doi.org/10.1002/2014JA020446

Wissing, J. M., Bornebusch, J. P., & Kallenrode, M. B. (2008). Variation of energetic particle precipitation with local magnetic time. *Advances in Space Research*, *41*(8), 1274–1278. https://doi.org/10.1016/j.asr.2007.05.063

Yando, K., Millan, R. M., Green, J. C., & Evans, D. S. (2011). A Monte Carlo simulation of the NOAA POES medium energy proton and electron detector instrument. *Journal of Geophysical Research: Space Physics*, *116*(A10), 10231. https://doi.org/10.1029/2011JA016671

Zawedde, A. E., Nesse Tyssøy, H., Stadsnes, J., & Sandanger, M. I. (2019). Are EEP events important for the tertiary ozone maximum? *Journal of Geophysical Research: Space Physics*, *124*(7), 5976–5994. https://doi.org/10.1029/2018JA026201

Zhang, J., Richardson, I., Webb, D., Gopalswamy, N., Huttunen, E., Kasper, J. C., et al. (2007). Solar and interplanetary sources of major geomagnetic storms ($Dst \leq -100$ nT) during 1996–2005. *Journal of Geophysical Research: Space Physics*, *112*(A10), A10102. https://doi.org/10.1029/2007JA012321